COMPARATIVE STUDY OF TENSILE PROPERTIES OF UNI-DIRECTIONAL SINGLE-TOW SIC-MATRIX COMPOSITES REINFORCED WITH VARIOUS NEAR-STOICHIOMETRIC SIC FIBERS

—K. Ozawa, Y. Katoh, E. Lara-Curzio, L.L. Snead (Oak Ridge National Laboratory), T. Nozawa (Japan Atomic Energy Agency)

OBJECTIVE

A procedure for evaluating mechanical properties of SiC/SiC mini-composite samples was established, with specific consideration of minimizing the personnel exposure during testing of radiological samples. In the course of the test procedure development, unirradiated CVI SiC matrix mini-composite samples reinforced with four different near-stoichiometric SiC fibers were evaluated.

SUMMARY

Four types of mini-composites (with variations in fiber and interphase but with the same SiC matrix) were evaluated for tensile and fiber/matrix interfacial properties. The composites reinforced with Hi-Nicalon™ Type-S (HNLS), Tyranno™-SA3 (SA3), experimental Sylramic™ and Sylramic-iBN fibers exhibited ultimate tensile stresses equivalent to ~77, ~53, ~69, and ~81% of the single fiber strength at 25 mm, respectively. The ultimate tensile stress appeared to increase with the estimated interfacial sliding stress, with the exception of the HNLS composite. The sliding stress increased with increasing fiber surface roughness. The HNLS composite exhibited the high tensile strength, likely because the very low interfacial sliding stress enabled global load sharing. The SA3 and Sylramic composites exhibited premature failure, attributed to the very high interfacial sliding stresses due primarily to the physical roughness of the fiber surfaces. More compliant interphases would optimize these fiber composites with unidirectional architecture.

PROGRESS AND STATUS

Introduction

Silicon carbide (SiC) -based ceramics and composites (SiC/SiC) are considered for applications in various components of fusion and advanced fission reactor systems and fuel assemblies, due primarily to their superior irradiation performance and thermo-physical, -chemical, and -mechanical properties [1, 2]. Continuous SiC-fiber, SiC-matrix composites are of particular importance for applications which require reliability, toughness, and near-net shape fabrication.

One focus of irradiation studies of SiC/SiC composites in the past few decades has been determination of the fundamental response of the materials produced with various constituent options and processing routes. Through this effort, composites containing near-stoichiometric SiC fibers, such as Tyranno™-SA3 (SA3) and Hi-Nicalon™ Type-S (HNLS), and high crystallinity SiC matrices produced by chemical vapor infiltration (CVI) or nano-infiltration and transient eutectic-phase (NITE) processes are found to possess acceptable irradiation stability. However, a design scheme for the optimum interphase for radiation service remains unresolved due primarily to the lack of understanding of the irradiation effects on the fiber/matrix interfacial properties.

The use of mini-composites, which are composites uni-directionally reinforced with a single fiber tow, is an appropriate approach for evaluating the interfacial properties [3]. The general advantages of the mini-composite approach are as follows: 1) due to its simple uni-directional fiber architecture, the in-situ fiber strength and interfacial properties can be determined in relatively simple ways [4, 5], and 2) a large number of specimens can be fabricated at a low cost in relatively a short time. Moreover, the very small volume of the mini-composite samples is attractive for irradiation studies due to the very high unit-volume cost of irradiation and the radiological concerns associated with the evaluation of irradiated material.

In the present work, a procedure for evaluating mechanical properties of SiC/SiC mini-composite samples was established at Oak Ridge National Laboratory, with specific consideration of minimizing the personnel exposure during testing of the radiological samples. In the course of the test procedure development, CVI SiC matrix mini-composite samples reinforced with four different near-stoichiometric SiC fibers were evaluated in the unirradiated condition.

Experimental Procedure

Materials

Table I describes the mini-composites; optical micrographs of polished cross sections of each mini-composite are shown in Fig. 1. In brief, four types of unidirectional single-tow mini-composites were prepared in this study. Tyranno-SA3, Hi-Nicalon Type-S, experimental Sylramic™ and experimental Sylramic™-iBN SiC fibers were used as reinforcement. The Sylramic-iBN, made from Sylramic, is a fiber with the excess boron used as a sintering aid removed from the fiber bulk. This boron formed a thin in-situ BN coating on the fiber surface, in order to improve thermo-structural and -chemical properties [6]. The unidirectional mini-composites were fabricated by the CVI process at Hyper-Therm High-Temperature Composites, Inc. (Huntington Beach, California). During the CVI process, the fiber bundle was held so that the cross sectional area of a mini-composite was minimized and the shape of the cross section was close to a circle, as shown in Fig. 1. The fiber/matrix (F/M) interphase was single layer pyrolytic carbon (PyC) with a nominal thickness of 150 nm. The PyC interphase coating was not applied to the experimental Syl-iBN composite. Hereafter, the IDs indicated in Table I (SA3 for Tyranno-SA3 (UD)/150nm-PyC/CVI, HNLS for Hi-Nicalon Type-S (UD)/150nm-PyC/CVI, Syl-PyC for experimental Sylramic (UD)/150nm-PyC/CVI, and Syl-iBN for experimental Sylramic-iBN (UD)//CVI mini-composite) are used in this paper.

Table I: Properties of mini-composites used in this study. Nominal mechanical properties of SiC fibers are also listed as supplied by the manufacturers.

ID	Fiber	Int.	Matrix	r [μm]	N	f [%]	σ_f [GPa]	E_f [GPa]	ε_f [%]
HNLS	Hi-Nicalon Type-S	150 nm PyC	CVI	12	500	45-50	2.6	420	0.6
SA3	Tyranno-SA3	150 nm PyC	CVI	7.5	1600	42-47	2.8	409	0.7
Syl-PyC	Exp-Sylramic	150 nm PyC	CVI	10	800	43-50	3.0	380	0.8
Syl-iBN	Exp-Sylramic-iBN	n/a	CVI	10	800	44-47	3.0	380	0.8

Int. denotes interphase, r the fiber diameter, N the number of filaments in a tow, f the fiber volume fraction, σ_f the single fiber strength at 25 mm, E_f the fiber modulus, ε_f the fiber elongation, *PyC* pyrolytic carbon, *CVI* chemical vapor infiltration, and *exp* experimental.

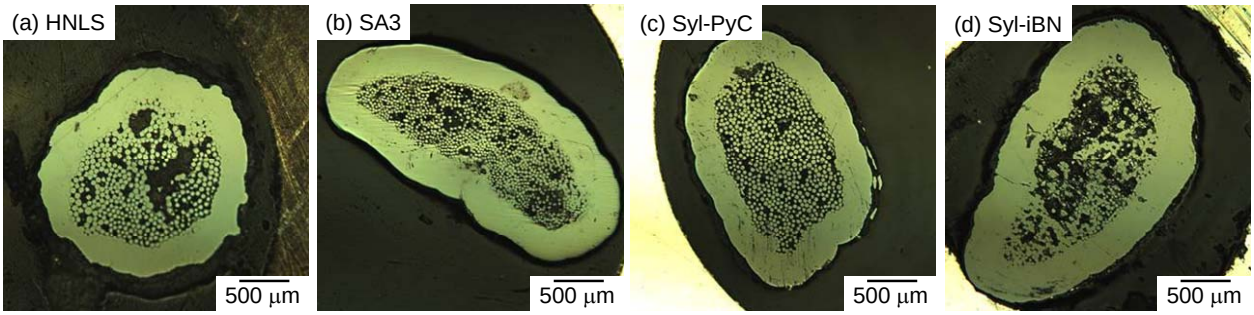

Figure 1: Optical micrographs of polished cross sections of (a) HNLS, (b) SA3, (c) Syl-PyC, and (d) Syl-iBN mini-composites.

Tensile Tests

The test apparatus is shown in Fig. 2. The tensile tests were conducted using an electromechanical testing machine (Insight 10, MTS Systems Co., Eden Prairie, Minnesota) with a load capacity of 10 kN. Strain was measured by a pair of linear variable differential transducers, LVDTs (Lucas Schaevitz GCA-121-125, Hampton, Virginia). We adopted an alignment system similar to the one used in single fiber tensile testing standardized in ASTM C 1557 in order to assure specimen alignment.

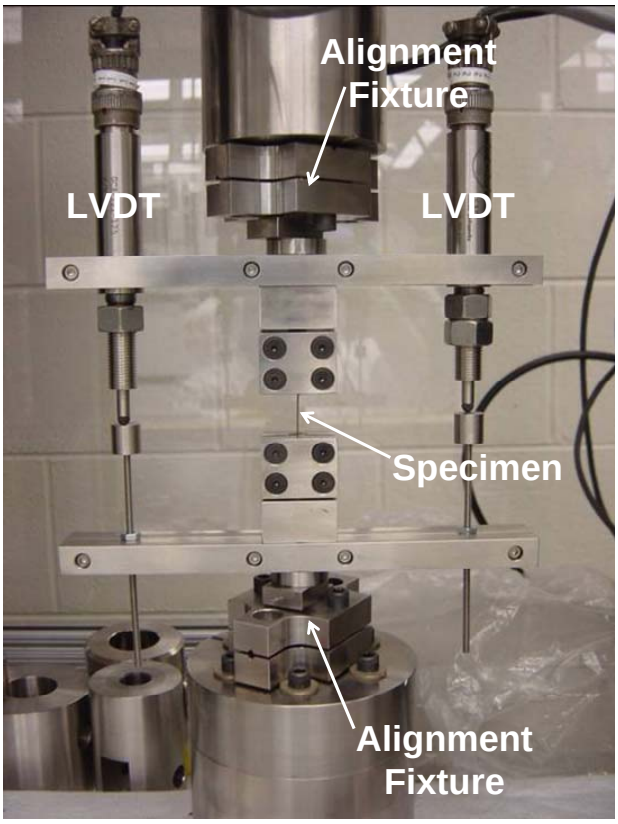

Figure 2: Mini-composite tensile test apparatus used in this study.

Figure 3 is a drawing of a specimen and aluminum tabs. A pair of aluminum tabs was fastened to the ends of a mini-composite sample using an epoxy adhesive dispersed by a syringe. In order to assure specimen alignment, the specimen to be glued was fixed in a V-notched fixture with flathead screws, as shown in Fig. 4. A polyethylene spacer sheet and/or the combination of a silicon release spray and a silicone remover were used to remove the specimen from the fixture after epoxy curing. This fixture including the specimen was cured at 110°C for more than 3 hours in an air furnace in order to develop the adhesive's maximum bonding strength. The gauge length of the specimens is 18 mm, defined by the distance between the inner ends of the aluminum tabs. Figure 5 shows the gripping fixture and the guide rail provided for alignment. The specimen was clamped into the simple V-notched fixtures with flathead screws. The guide rail was used to confirm specimen alignment and to avoid damaging the specimen during handling.

The tests were conducted at ambient conditions under crosshead displacement control at 0.1 mm/min. Unloading/reloading cyclic tensile tests were conducted to evaluate interfacial properties. Previous to the tensile tests, compliance of the grip assembly was determined using a set of tungsten wires with various gauge lengths. As a result, the system compliance of 1.32×10^2 μm/N was obtained as shown in Fig. 6. Tensile strain is determined by the following equation, $\varepsilon = (\Delta L - C_S P)/L_0$, where ε is the tensile strain, ΔL the average cross-head displacement recorded by LVDTs, C_S the system compliance, P the applied load, and L_0 the gauge length. The fiber volume fraction (f) of the mini-composites was determined by a combination of optical microscopy and image analysis. It is noted that some errors may have been introduced due to surface damage during polishing. The mini-composite tensile stress (σ) is defined by $\sigma = P/(\pi r^2 N/f)$, with r the average fiber radius, and N the number of filament in a tow. The proportional limit load or proportional limit stress (PLL or PLS) was defined as the stress at 0.5% deviation from the extrapolated fit of the slope by the least squares method for the initial loading.

After the tensile tests, the fracture surfaces of the specimens were examined using a scanning electron microscope (SEM, Topcon SM-510, Paramus, New Jersey). Fiber pull-out length and matrix crack spacing were also measured, in order to estimate the interfacial sliding stress. This study included only tensile tests on unirradiated composites, but identical procedures will be used in experiments on irradiated material.

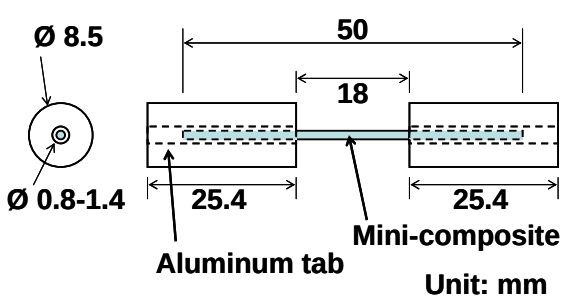

Figure 3: Dimension of a mini-composite and a pair of aluminum tabs.

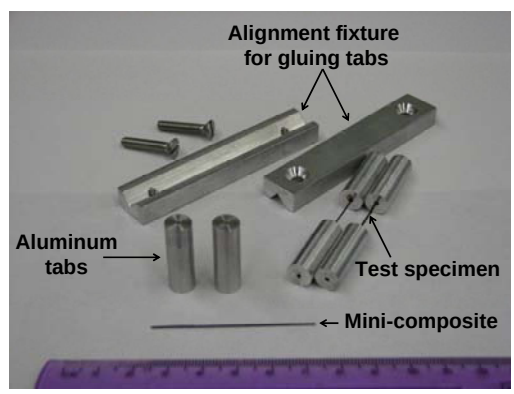

Figure 4: Mini-composite, aluminum tabs and alignment fixture for gluing tabs.

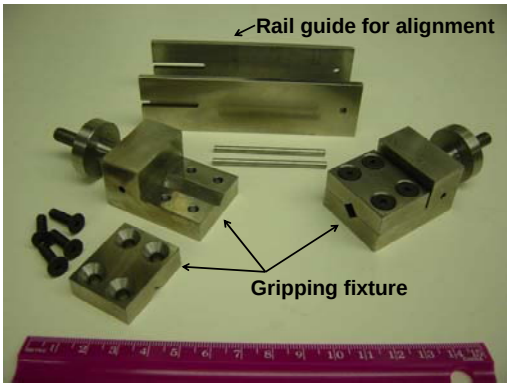

Figure 5: Gripping fixture and rail guide for specimen alignment.

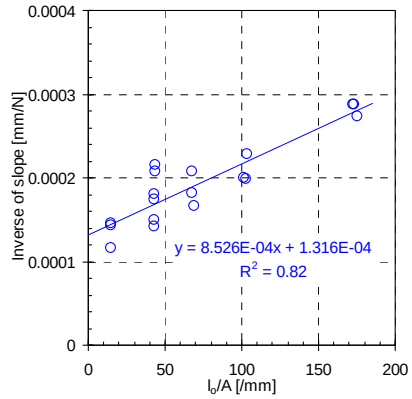

Figure 6: Machine compliance of the mini-composite tensile system. l_0 and A denote the gauge length and the cross-sectional area of the specimen.

Results and Discussion

Tensile Load-Strain Responses

Representative load-tensile strain curves for the four mini-composites are shown in Fig. 7, and the mechanical properties of the mini-composites are listed in Table II. As shown in Fig. 7 (a), the HNLS mini-composites exhibited a typical pseudo-ductile fracture behavior; there was an initial steep linear region in the load-strain curve, with a second, nearly linear region at higher strains, repeated during tensile loading with multiple unloading-reloading sequences. The initial linear portion corresponds to the linear elastic deformation of the mini-composite, whereas the second linear portion corresponds to a process of progressive development and opening of multiple matrix micro-cracks. The SA3 mini-composites exhibited more brittle behavior, with narrower hysteresis loop width (~0.02%) and smaller elongation after the PL (an average of 0.174% for the fracture strain), compared to the HNLS mini-composites. The Syl-PyC and Syl-iBN composites exhibited rather brittle failure. The overall behavior of these mini-composites is similar to the SA3 mini-composite, implying fiber properties comparable to Tyranno-SA3 at room temperature. Of importance is the fiber strength (the RS values in Table II.). In the overall composite strength, 69% of Sylramic and 81% of Sylramic-iBN fiber strength was achieved in the mini-composite system; this compares the HNLS (77%) and the SA3 (53%). This result indicates that the experimental fibers are capable of bearing loads similar to the two near-stoichiometric SiC fibers which are currently commercially available.

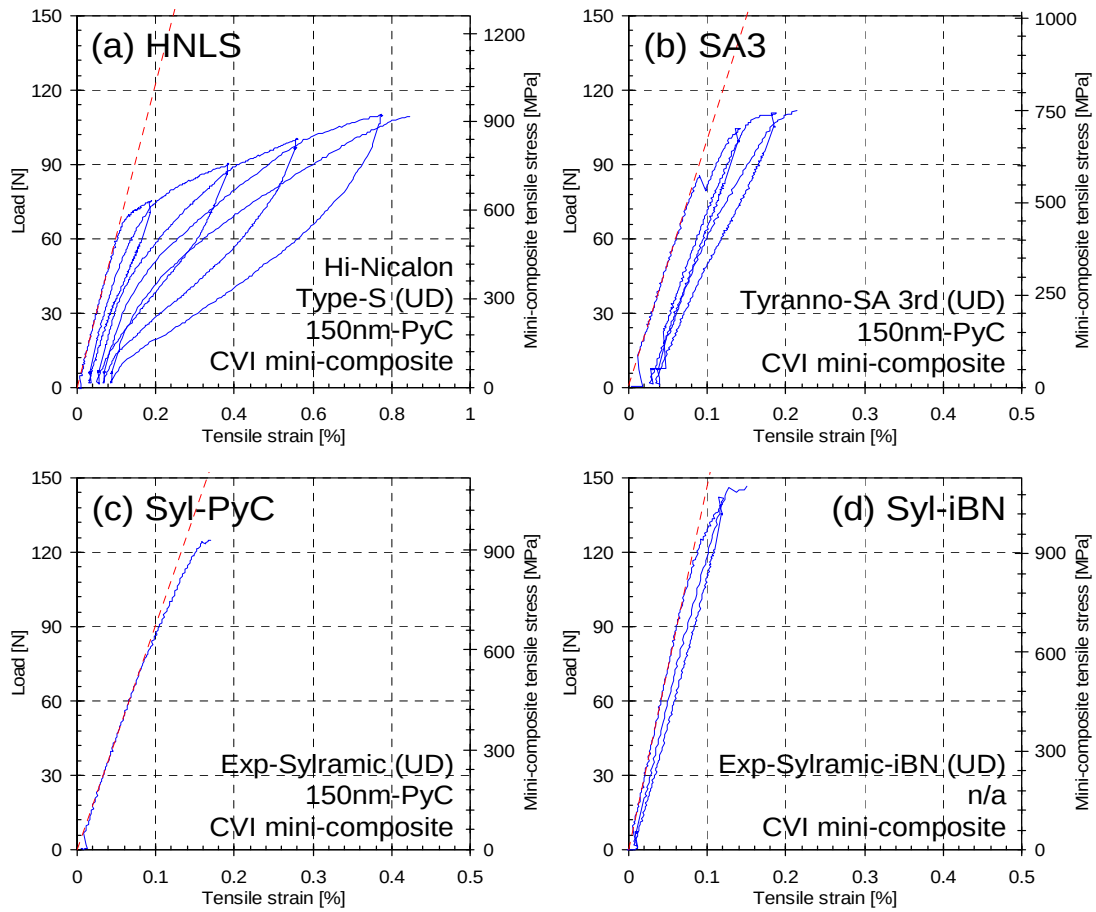

Figure 7: Representive tensile load-strain curves for (a) HNLS, (b) SA3, (c) Syl-PyC, and (d) Syl-iBN mini-composites. Note that the tensile strain axis is different for each mini-composite.

Table II: Tensile test results for the mini-composites. Numbers in parenthesis show standard deviations.

ID	Fiber	Int.	Matrix	P_{fr} [N]	P_P [N]	ε_{fr} [%]	ε_P [%]	σ_U [MPa]	σ_P [MPa]	σ^T [MPa]	RS [%]	#
HN LS	Hi-Nicalon Type-S	150 nm PyC	CVI	113 (5)	67 (4)	0.877 (0.029)	0.152 (0.011)	923 (31)	552 (34)	-303 (75)	77 (3)	4
SA3	Tyranno-SA3	150 nm PyC	CVI	105 (6)	80 (8)	0.270 (0.072)	0.114 (0.041)	676 (52)	513 (51)	-110 (121)	53 (3)	4
Syl-PyC	Exp-Sylramic	150 nm PyC	CVI	130 (7)	91 (11)	0.201 (0.044)	0.121 (0.006)	958 (40)	675 (91)	-73 (-)	69 (4)	2
Syl-iBN	Exp-Sylramic-iBN	n/a	CVI	153 (10)	112 (18)	0.174 (0.033)	0.099 (0.012)	1115 (17)	819 (168)	0 (-)	81 (5)	2

P_{fr} denotes the load at fracture, P_P the load at proportional limit (PL), ε_{fr} the strain at fracture, ε_P the strain at PL, σ_U the ultimate tensile strength, σ_P the PL stress, σ^T the misfit stress, RS the relative strength of the mini-composite to the single fiber strength, and # the number of tests.

SEM observation

Figure 8 shows SEM images of the fracture surface of each mini-composite. Table III lists the result of the

average fiber pull-out length determination. Shorter pull-out lengths (~100 μm) were measured in SA3 and Syl-PyC compared to the HNLS (~300 μm), while very short pull-out length (~15 μm) was obtained in Syl-iBN (HNLS > SA3 ~ Syl-PyC > Syl-iBN). In order to measure the matrix crack spacing, the fractured specimen was mounted on a glass platen with an epoxy adhesive and polished longitudinally, but unfortunately typical matrix crack spacing could not be detected for all specimens using an optical microscope. It is believed that such typical transverse matrix cracks were not seen along the whole specimen due to the premature failure before the matrix loading reached saturation in these composite systems. Therefore, the matrix crack spacing in a fiber bundle or the distance of crack deflection near a fracture surface were used as the matrix crack spacing in this study. Examples of these determinations are shown in Fig. 9.

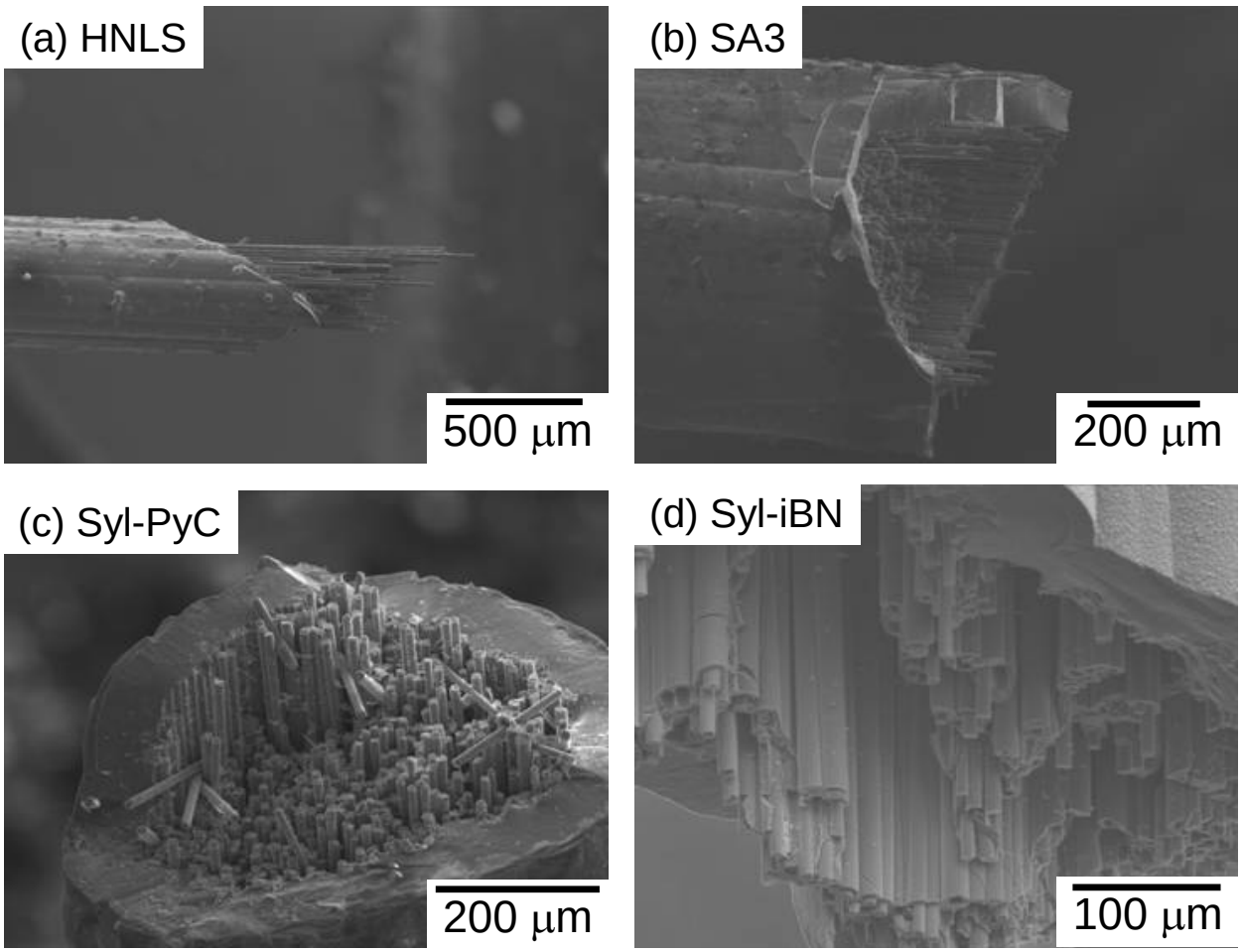

Figure 8: SEM micrographs of the fracture surfaces of the (a) HNLS, (b) SA3, (c) Syl-PyC, and (d) Syl-iBN mini-composites.

Table III: Results of the average fiber pull-out length, the average matrix crack spacing, and the interfacial sliding stress from the hysteresis loop analysis for the mini-composites.

	l_p [um]	d [μm]	τ from Eq. (1) [MPa]	τ from Eq. (2) [MPa]	τ from Eq. (3) [MPa]
HNLS	300	~400	5	8	11-14
SA3	100	~100	85	15	15-20
Syl-PyC	100	~200	170	16	28-37
Syl-iBN	15	~50	950	73	219-287

l_p, d, τ denote the average fiber pull-out length, the average matrix crack spacing, and the interfacial sliding stress, respectively.

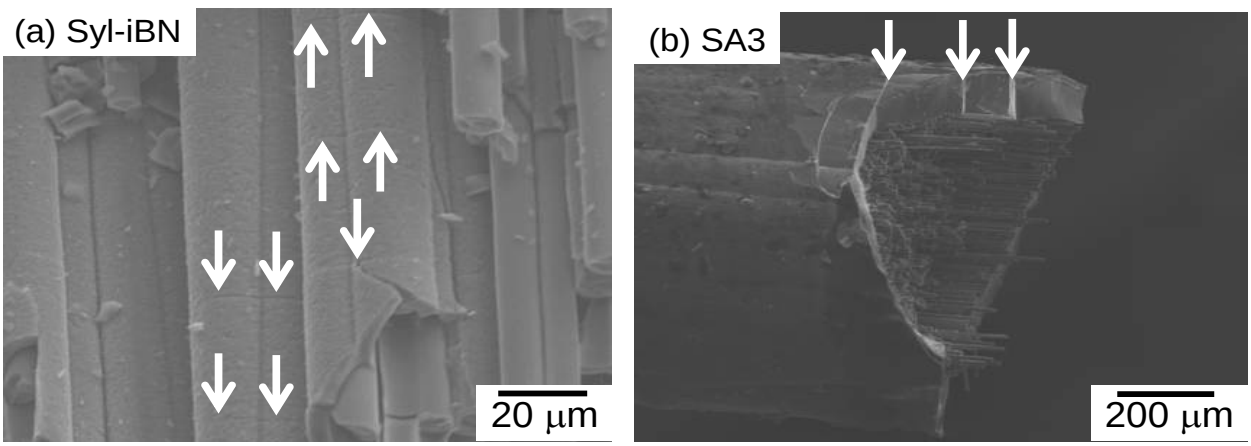

Figure 9: Examples of matrix crack spacing determination. (a) Matrix crack spacing in the fiber bundle for Syl-iBN, and (b) distance between the crack deflection at outer SiC layer for SA3.

Interfacial Sliding Stress

The interfacial sliding stress (τ) was estimated from the hysteresis loop width, the matrix crack spacing, and the fiber pull-out length. First, in the hysteresis loop analysis by Lamon *et al.* [4] and Vagaggini *et al.* [5], the interfacial sliding stress (τ) can be obtained from the following equation [4]:

$$\tau = \frac{b_2(1-a_1 f)^2}{2 f^2 E_m}\left(\frac{r}{d}\right)\left(\frac{\sigma_p^2}{d\varepsilon}\right)\left(\frac{\sigma}{\sigma_p}-\frac{\sigma_{\min}}{\sigma_p}\right)\left(1-\frac{\sigma}{\sigma_p}\right) \quad (1)$$

where a_1 and b_2 are the Hutchinson-Jensen parameters [7], E_m the matrix modulus, d the average matrix crack spacing, $d\varepsilon$ the hysteresis loop width, σ_p the peak stress of the hysteresis loop, σ the stress where $d\varepsilon$ is measured, and σ_{min} the minimum stress of the hysteresis loop. τ was determined from the hysteresis loop immediately prior to failure, assuming the same matrix crack spacing at the failure of the composite systems.

τ is also estimated using the matrix crack spacing, expressed as [8]:

$$\tau = \frac{\sigma_S r E_m (1-f)}{2dEf} \tag{2}$$

where σ_S is the applied stress at matrix cracking saturation. The observed result of the matrix crack spacing suggests that the mini-composites fractured before reaching matrix crack saturation, therefore the ultimate tensile stress was taken as σ_S for convenience.

The third method for estimating τ is to use the fiber pull-out length. Curtin derived the following equation to estimate the interfacial sliding stress [9]:

$$\tau = \frac{r\lambda(m)\sigma_c}{4l_p} \tag{3}$$

where l_p is the average fiber pull-out length, σ_c and m the in-situ fiber fracture strength and the Weibull modulus, respectively, and $\lambda(m)$ is the known function of Weibull modulus as $\lambda(m) \approx 0.716 + 1.36/m^{0.6}$ for $m \geq 1$ [10], In this paper the fiber strength at fracture is used for the in-situ fiber fracture strength. There is limited data about the Weibull modulus of in-situ SiC fiber strength, but m=3-9 is assumed in Eq. (3), according to the references on in-situ strength of similar SiC fibers [10, 11].

All results for the interfacial sliding stress are shown in Table III. A relatively low value of τ is obtained for the HNLS composite and very high τ values were derived for the three other composites. Because of the relatively brittle failure experienced by these composites, it is likely that the τ values were not correctly determined. However, it is noted that the ranking of the τ values seems to be qualitatively reasonable as they are inversely correlated with the fiber pull-out length (HNLS < SA3 ~ Syl-PyC < Syl-iBN).

The three analytical methods gave very major differences in τ values. During the unloading-reloading processes in the tensile testing, as seen in Fig. 7, the stable interfacial sliding was not achieved with the exception of the HNLS composite. In such a case, it is known that the hysteresis loop analysis gives an unrealistically large sliding stress value. In the matrix crack spacing analysis, the ultimate tensile strength was used to estimate the sliding stress instead of using the stress for matrix crack saturation. Because the matrix crack saturation was obviously not achieved at the failure of the non-HNLS composites, this may have caused a slight underestimation of the sliding stress values. For the method based on the fiber pull-out length, the estimated sliding stress values may suffer substantial errors due to uncertainty in the pull-out length determination. Thus, the τ values in Table III are considered to have only qualitative significance, although those determined from the matrix crack spacing seem to be most realistic.

The interfacial sliding stress (τ is essentially the frictional stress at the sliding interface, thus should macroscopically be a product of the clamping stress and the interfacial frictional coefficient, which is closely related to the fiber surface roughness. The experimental observations with on τ values and the fiber surface roughness are summarized in Table IV. The relative value of τ is clearly dependent on the micro-topological features of the fiber surface.

Table IV: The relationship between microstructure, fiber roughness, and interfacial sliding stress of near-stoichiometric SiC fibers.

Fiber	Hi-Nicalon Type-S	Tyranno-SA3	Exp-Sylramic	Exp-Sylramic-iBN
Surface Micro-structure		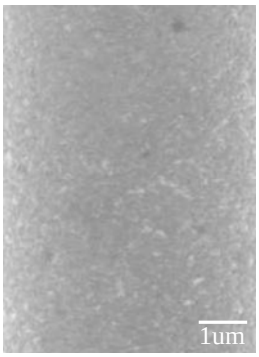	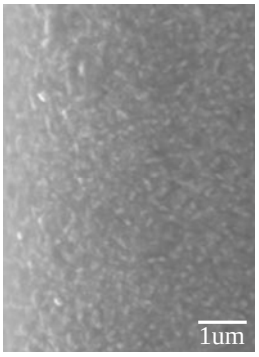	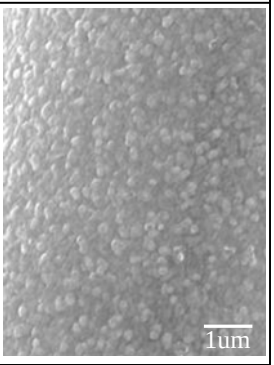
R_q [nm]	•0.87, Hinoki (2001) •2.33, Sauder *et al.* (2010) •<10, Yun *et al.* (2001)	•1.71, Hinoki (2001) •8.04, Sauder *et al.* (2010)	•~10, Yun *et al.* (2001) •17.561, Brennan (2000)	•~27, Yun *et al.* (2001)
τ [MPa]	•8, This work •14.46, Sauder *et al.* (2008)	•15, This work •223, Sauder *et al.* (2008)	•16, This work	•73, This work
Interphase	•150 nm PyC	•150 nm PyC	•150 nm PyC	•n/a (Sylramic-iBN)

R_q denotes the root mean square fiber surface roughness. References are from [6, 12-14] for the fiber roughness, and from [15] for the interfacial sliding stress.

The clamping stress, or the compressive radial stress at the interface, generally results from a combination of the mismatch in coefficient of thermal expansion (CTE) between the fiber and the matrix (possibly involving the interphase), the physical roughness of the interface, and the compliance and strength of the interphase. We have considered the clamping stress in each mini-composite system qualitatively. The clamping stress (σ_{CL}) is expressed by the following equation [16],

$$\begin{aligned}\sigma_{CL} &\sim \sigma_{CTE} + \sigma_R \\ &= \sigma_{CTE} + \frac{E_m E_f}{E_f(1+\nu_m) + E_m(1-\nu_f)}\left(-\frac{A}{r}\right)\end{aligned} \tag{4}$$

where σ_{CTE} and σ_R are the residual stress induced by CTE mismatch and the contribution of fiber roughness, the ν_m, ν_f are the Poisson's ratios of the matrix and fiber, E_f the Young's modulus of a fiber, and A the characteristic amplitude of roughness along the debonded interface. Figure 10 shows the calculated results for the residual stress of each composite system, and Table V gives the calculated result for the clamping stress in each composite system. The four phase model [17] was used to estimate σ_{CTE}. For calculation, ν_m, ν_f and A were assumed to be 0.2, 0.2 and $2R_q$, where R_q is the root mean square fiber surface roughness. The thickness of the BN layer on the Sylramic-iBN fiber was assumed to be 200 nm [6]. As shown in Table V, the contribution of fiber surface roughness is much larger than the CTE mismatch. Additionally, the clamping stress is strongly affected by the fiber surface roughness. This trend of the calculated clamping stress qualitatively corresponds to the misfit stress as described below. Therefore, it is concluded that the relationship of the tensile properties of the mini-composites studied is mainly attributed to the difference in the fiber surface roughness.

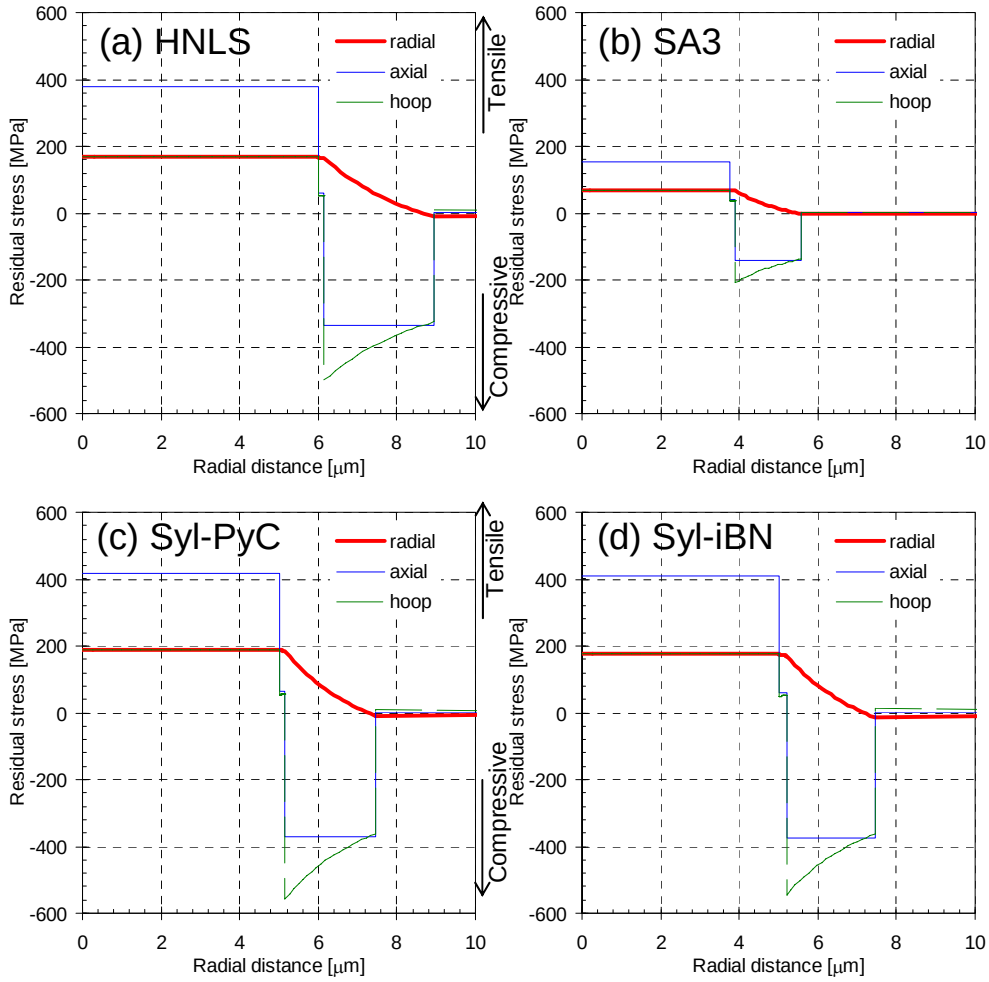

Figure 10: Residual stress analysis result for (a) HNLS, (b) SA3, (c) Syl-PyC, and (d) Syl-iBN composite, using the four phase model.

Table V: Calculated results of the radial residual stress by CTE mismatch (σ_{CTE}), the compressive stress caused by fiber surface roughness (σ_R), and the clamping stress (σ_{CL}). Note that negative value ($\sigma < 0$) denotes compressive stress.

	σ_{CTE} [MPa]	σ_R [MPa]	σ_{CL} [MPa]
HNLS	167	-172	-5
SA3	69	-939	-871
Syl-PyC	188	-1490	-1302
Syl-iBN	175	-2291	-2116

Misfit Stress (σ^T)

The misfit stress of each mini-composite was also measured using regression analysis of the tensile reloading segments, using the method derived by Steen *et al.* [18] (Table II). It is noted that negative misfit stress ($\sigma^T<0$) denotes compressive axial residual stress in the matrix and tensile residual stress in the radial direction. As shown in Table II, the larger σ^T values were obtained for the SA3, Syl-PyC, and Syl-iBN composites compared to the HNLS composites (HNLS < SA3 < Syl-PyC < Syl-iBN ~ 0).

Ultimate Tensile Strength (UTS)

The tensile properties of a unidirectional composite system are strongly affected by the Weibull modulus (m), the characteristic strength (σ_0) of the fibers, and the interfacial sliding stress (τ). Under the assumption of the global load sharing (GLS) theory of Curtin [19], the fiber-averaged UTS ($\sigma_{U,f}$) in a unidirectional composite system is expressed as follows:

$$\sigma_{U,f}^{GLS} = \left(\frac{\sigma_0^m \tau L_0}{r}\right)^{\frac{1}{m+1}} \left[\frac{2(m+1)}{(m+2)m}\right]^{\frac{1}{m+1}} \left(\frac{m+1}{m+2}\right) \tag{5}$$

Figure 11 compares the fiber-averaged UTS results accompanied by the $\sigma_{U,f}^{GLS}$ strength calculated according to this theory. The interfacial sliding stress from the matrix crack spacing was used for τ. The Weibull modulus was assumed to be ~6.2 for HNLS [15, 20], 8.2 for SA3 [15], and 4.21 for the two experimental Sylramic fibers [21]. The fiber-averaged UTS of HNLS appeared to agree with the value calculated from the GLS theory. In contrast, this theory largely overestimates the fiber-averaged UTS for the three other composites. It is likely that, in these composites, the global load sharing is not achieved before fracture but the fracture is governed by the local load sharing (LLS), due to their relatively high interfacial sliding stress (Hence the use of Sylramic-iBN fiber without any interfacial coating in unidirectional architecture is generally not recommended due to the high fiber surface roughness (Ref. [6] and Table IV)). Based on one of the simplest LLS models, Zweben derived the following relationship for the fiber-averaged UTS of uni-directional composites [22]:

$$\sigma_{U,f}^{LLS} = \sigma_0 \left(\frac{L_0(m-1)}{LNm}\right)^{\frac{1}{m+1}} \tag{6}$$

where L is also the gauge length of the mini-composite. In this model, the early fiber failures tend to initiate catastrophic failure of the composite. Hence it is noted that this can be regarded as a lower bound on the composite strength. Figure 11 also shows the $\sigma_{U,f}^{LLS}$ calculated using Eq. (6). These values underestimate the experimental data. However, the difference between the fiber-averaged UTS and the $\sigma_{U,f}^{LLS}$ may be reasonable since the fracture mode is different. The calculated $\sigma_{U,f}^{LLS}$ are the values under the assumption of catastrophic (brittle) fracture. However, the three composites actually fractured with pseudo ductile behavior as shown in Fig. 8. The part of the specimen where this pseudo ductile fracture has occurred should contribute to the increase of the composite strength.

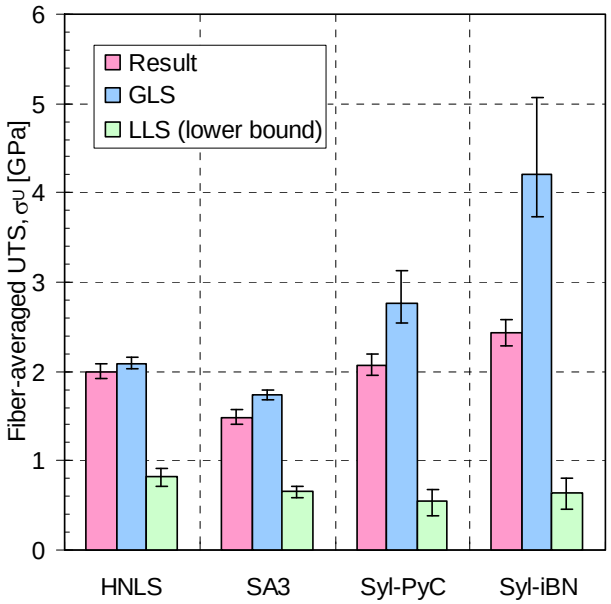

Figure 11: Fiber-averaged UTS compared with the two models. The error bars indicate the standard deviation for the result and ±1 change in the Weibull modulus for the GLS and the LLS.

Acknowledgement

The experimental Sylramic and Sylramic-iBN fibers used in this study were supplied by COI Ceramics, Inc. (San Diego, California). This research was sponsored by the Office of Fusion Energy Sciences, US Department of Energy under contract DE-AC05-00OR22725 with UT-Battelle, LLC.

References

[1] T. Nozawa, T. Hinoki, A. Hasegawa, A. Kohyama, Y. Katoh, L.L. Snead, C.H. Henager Jr, J.B.J. Hegeman, J. Nucl. Mater. 386-388 (2009) 622.
[2] Y. Katoh, L.L. Snead, C.H. Henager Jr, A. Hasegawa, A. Kohyama, B. Riccardi, H. Hegeman, J. Nucl. Mater. 367-370 (2007) 659.
[3] R. Naslain, J. Lamon, R. Pailler, X. Bourrat, A. Guette, F. Langlais, Composites Part A: Applied Science and Manufacturing 30 (1999) 537.
[4] J. Lamon, F. Rebillat, A.G. Evans, J. Am. Ceram. Soc. 78 (1995) 401.
[5] E. Vagaggini, J.-M. Domergue, A.G. Evans, J. Am. Ceram. Soc. 78 (1995) 2709.
[6] H.M. Yun, J.Z. Gyekenyesi, Y.L. Chen, D.R. Wheeler, J.A. DiCarlo, Ceram. Eng. Sci. Proc. 22 (2001) 521.
[7] J.W. Hutchinson, H.M. Jensen, Mech. Mater. 9 (1990) 139.
[8] F.W. Zok, S.M. Spearing, Acta Metallurgica et Materialia 40 (1992) 2033.
[9] W.A. Curtin, J. Am. Ceram. Soc. 77 (1994) 1075.
[10] I.J. Davies, T. Ishikawa, M. Shibuya, T. Hirokawa, Compos. Sci. Technol. 59 (1999) 801.
[11] S. Guo, Y. Kagawa, J. Eur. Ceram. Soc. 22 (2002) 2349.
[12] T. Hinoki, "Investigation of Mechanical Properties and Microstructure of SiC/SiC Composites for Nuclear Application, " Doctoral Thesis, Kyoto University (2001).
[13] C. Sauder, A. Brusson, J. Lamon, International Journal of Applied Ceramic Technology 7 (2010) 291.
[14] J.J. Brennan, Acta Materialia 48 (2000) 4619.

[15] C. Sauder, A. Brusson, J. Lamon, Ceram. Eng. Sci. Proc. 29 (2008) 91.
[16] R.J. Kerans, T.A. Parthasarathy, J. Am. Ceram. Soc. 74 (1991) 1585.
[17] Y. Mikata, M. Taya, J. Compos. Mater. 19 (1985) 554.
[18] M. Steen, J.L. Valles, ASTM Special Technical Publication 1309 (1997) 49.
[19] W.A. Curtin, B.K. Ahn, N. Takeda, Acta Materialia 46 (1998) 3409.
[20] T. Nozawa, T. Hinoki, L.L. Snead, Y. Katoh, A. Kohyama, J. Nucl. Mater. 329-333 (2004) 544.
[21] M.C. Osborne, C.R. Hubbard, L.L. Snead, D. Steiner, J. Nucl. Mater. 253 (1998) 67.
[22] C. Zweben, AIAA J. 6 (1968) 2325.